




# Performance of SAR Polarimetric Calibration Using Hybrid Corner Reflectors: Numerical Simulations and Experimental Measurements

Suyun Wang , Kun-Shan Chen , *Fellow, IEEE*, and Motoyuki Sato , *Fellow, IEEE*

**Abstract**—In this article, we devise a polarimetric calibration method utilizing only three types of calibration targets, i.e., trihedral, dihedral, and a 22.5°-rotated dihedral corner reflectors and requiring no assumptions on the scene statistics. The influence of the roll angle in a 22.5°-rotated dihedral corner reflector is assessed by a full-wave numerical simulation. The effectiveness and accuracy of the method are verified with a ground-based synthetic aperture radar system and an airborne L-band Pi-SAR data. We demonstrate that an amplitude error as low as 0.5 dB and a phase error within 3° can be achieved, showing an excellent agreement between the theoretical and calibrated polarimetric signatures for the reference targets. We further exploit the calibration on the Pauli decomposition, Yamaguchi four-component decomposition, and the estimation of the polarimetric parameters derived from target scattering vector method decomposition to show the superior performance of the devised calibration method.

**Index Terms**—Corner reflector, GB-SAR, Pi-SAR, polarimetric calibration, polarimetric decomposition.

## I. INTRODUCTION

FULLY polarimetric synthetic aperture radar (PolSAR) has been widely applied in a wide range of terrain classification, geophysical parameter retrieval, and target detection, to name a few [1], [2]. However, the advantages of a fully PolSAR can only be exploited after an accurate polarimetric calibration has been done [3]. In measuring a target scattering matrix, the received signals consist of the desired target scattering matrix and the transmission and reception defects of the measurement system. Polarimetric calibration is devised to correct the polarization distortions caused by an imperfect radar system, which are primarily due to a nonideal channel imbalance and polarization cross-talk errors between the transmitter and receiver [4].

Various polarimetric calibration methods have been proposed and well documented in numerous papers [5]–[10]. Generally, calibration techniques can be grouped into two categories based

on the type of reference target: 1) point-target-based [11]–[13], and 2) distributed-target-based [14]–[16].

Among the point-target calibration techniques, Whitt *et al.* [5] proposed a method that uses three calibration targets without distortion matrices assumptions and is resolved using an eigenvalue approach. Freeman *et al.* [11] developed a technique that includes three polarimetric active radar calibrators within the imaged scene to derive the target scattering matrix. Fujita *et al.* [13] used selective corner reflectors (CRs) to perform polarimetric calibration for spaceborne and airborne SAR systems. Sarabandi *et al.* [17] improved this technique by employing a conducting sphere and depolarizing calibration targets to determine the distortion parameters. Yueh *et al.* [18] summarized the conditions for the scattering matrices of the calibration targets. The abovementioned group of algorithms is relatively simple and broadly applicable; however, the sensitivity to the positioning of the calibration targets needs to be carefully accounted for, which also holds for the method proposed in this article.

Among the distributed-target calibration techniques, Van Zyl [7] developed a unified algorithm that uses at least one trihedral CR and a distributed target under the assumption that azimuth symmetry holds. Quegan [16] utilized the distributed targets to compensate for cross-talk without an assumption about the system reciprocity. Shimada [19] applied an incoherent decomposition model to the uncalibrated covariance data measured for the distributed targets and subsequently estimated the polarimetric distortion matrix. Touzi and Shimada [20] used the distributed targets to correct the system gain and channel imbalance. These authors then used the target tilt angles of significant symmetric scattering for the calibration and validation of Phased Array type L-band SAR (PALSAR) polarimetric modes. Klein [14] presented a method to calibrate PolSAR data in the scattering matrix format that relies on backscatter reciprocity and the absence of a correlation between the copolarized and the cross-polarized acquisitions in distributed targets. Kimura [21] presented a new calibration method that uses the polarization orientation induced in built-up areas and applied it to PALSAR polarimetric calibration, invoking the reflection symmetry on the target. Ainsworth *et al.* [22] presented a concept of orientation angle preservation and proposed a method to use polarization orientation angles in built-up areas; this is an a posteriori method to calibrate the PolSAR data using the scattering reciprocity as the least constrained condition for the associated PolSAR system. This

Manuscript received January 30, 2020; revised May 18, 2020 and September 12, 2020; accepted October 24, 2020. Date of publication November 9, 2020; date of current version January 6, 2021. This work was supported in part by JSPS Grant-in-Aid for Scientific Research (A) under Grant 26249058. (Corresponding author: Suyun Wang.)

Suyun Wang is with Graduate School of Environmental Studies, Tohoku University, Sendai 980-8579, Japan (e-mail: metaphor.wsy@gmail.com).

Kun-Shan Chen is with College of Geomatics and Geoinformation, Guilin University of Technology, Guilin 541004, China (e-mail: chenks@radi.ac.cn).

Motoyuki Sato is with Center for Northeast Asian Studies, Tohoku University, Sendai 980-8576, Japan (e-mail: motoyuki.sato.b3@tohoku.ac.jp).

Digital Object Identifier 10.1109/JSTARS.2020.3036392

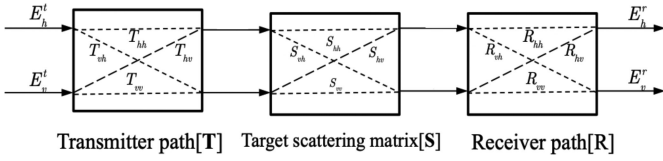


Fig. 1. Process for measuring the target scattering matrix.

second group of algorithms is stable but sometimes difficult to implement, if not always, as it requires that a relatively large homogeneous and stable distributed target be attainable and that scattering reciprocity and reflection symmetry be satisfied.

Given the abovementioned development of the calibration techniques, in this article, we present a general polarimetric calibration technique using hybrid CRs, requiring only one trihedral and two dihedral CRs with different rotation angles for polarimetric calibration. It is simple and makes no assumptions. Rest of this article is organized as follows. Section II describes the basics of polarimetric calibration, the calibration model, and the solution to the calibration matrix that will be used to calibrate the polarimetric SAR data. Section III presents the polarimetric calibration via numerical simulation, which is followed by a discussion of the calibration performance with error analysis. The impact of the roll angle on the performance of the 22.5°-rotated dihedral CR is also assessed. The polarimetric calibration experiment carried out for a GB-SAR system is presented in Section IV. Section V provides the results of polarimetric calibration in the context of an *L*-band airborne Pi-SAR data and compares the polarimetric signatures of reference targets before and after calibration. In addition, we come up to process the after-calibration Pi-SAR data with Pauli decomposition, Yamaguchi decomposition, and TSVM decomposition to examine the relationship between their performances and calibration quality. Finally, Section VI concludes this article.

## II. CALIBRATION ALGORITHM

In a practical, nonideal PolSAR system, there are inherent polarization cross-talk errors and channel imbalance between transmitter and receiver. In Fig. 1,  $E_h^t$  and  $E_v^t$  denote the horizontal and vertical polarization components of the incident field, respectively; similarly,  $E_h^r$  and  $E_v^r$  are the horizontal and vertical polarization components of the scattered field;  $T_{hh}$ ,  $T_{vv}$ ,  $R_{hh}$ ,  $R_{vv}$  represent channel imbalance and  $T_{hv}$ ,  $T_{vh}$ ,  $R_{hv}$ ,  $R_{vh}$  the cross talk. The wave propagation in the course of transmitting and receiving causes the target scattering matrix  $\mathbf{S}$  to be distorted to a measured scattering matrix. The goal of the polarimetric calibration is to recover, as fully as possible, the target scattering matrix  $\mathbf{S}$  from the measured scattering matrix.

### A. Signal Model

In Fig. 1, in a PolSAR system, the measured scattering matrix  $\mathbf{S}^m$  and theoretical scattering matrix  $\mathbf{S}^t$  are related by

$$\mathbf{S}^m = \mathbf{R}\mathbf{S}^t\mathbf{T} + \mathbf{N} \quad (1)$$

where  $\mathbf{S}^m$  and  $\mathbf{S}^t$  denote the measured and theoretical  $2 \times 2$  scattering matrices, respectively;  $\mathbf{T}$  and  $\mathbf{R}$  represent the transmitting and receiving distortion matrices, respectively, and  $\mathbf{N}$  accounts for random noise. Their expressions are as follows:

$$\mathbf{T} = \begin{bmatrix} \mathbf{T}_{hh} & \mathbf{T}_{hv} \\ \mathbf{T}_{vh} & \mathbf{T}_{vv} \end{bmatrix} \quad \mathbf{R} = \begin{bmatrix} \mathbf{R}_{hh} & \mathbf{R}_{hv} \\ \mathbf{R}_{vh} & \mathbf{R}_{vv} \end{bmatrix}$$

$$\mathbf{N} = \begin{bmatrix} \mathbf{N}_{hh} & \mathbf{N}_{hv} \\ \mathbf{N}_{vh} & \mathbf{N}_{vv} \end{bmatrix} \quad \mathbf{S} = \begin{bmatrix} \mathbf{S}_{hh} & \mathbf{S}_{hv} \\ \mathbf{S}_{vh} & \mathbf{S}_{vv} \end{bmatrix}. \quad (2)$$

Based on the aforementioned expressions, (1) can be rewritten as

$$\begin{bmatrix} \mathbf{S}_{hh}^m & \mathbf{S}_{hv}^m \\ \mathbf{S}_{vh}^m & \mathbf{S}_{vv}^m \end{bmatrix} = \begin{bmatrix} \mathbf{R}_{hh} & \mathbf{R}_{hv} \\ \mathbf{R}_{vh} & \mathbf{R}_{vv} \end{bmatrix} \begin{bmatrix} \mathbf{S}_{hh}^t & \mathbf{S}_{hv}^t \\ \mathbf{S}_{vh}^t & \mathbf{S}_{vv}^t \end{bmatrix} \begin{bmatrix} \mathbf{T}_{hh} & \mathbf{T}_{hv} \\ \mathbf{T}_{vh} & \mathbf{T}_{vv} \end{bmatrix} + \begin{bmatrix} \mathbf{N}_{hh} & \mathbf{N}_{hv} \\ \mathbf{N}_{vh} & \mathbf{N}_{vv} \end{bmatrix}. \quad (3)$$

Multiplying (3) and transferring it into a vector form results in

$$\begin{bmatrix} \mathbf{S}_{vv}^m \\ \mathbf{S}_{hh}^m \\ \mathbf{S}_{vh}^m \\ \mathbf{S}_{hv}^m \end{bmatrix} = \begin{bmatrix} \mathbf{R}_{vv}\mathbf{T}_{vv} & \mathbf{R}_{vh}\mathbf{T}_{hv} & \mathbf{R}_{vv}\mathbf{T}_{hv} & \mathbf{R}_{vh}\mathbf{T}_{vv} \\ \mathbf{R}_{hv}\mathbf{T}_{vh} & \mathbf{R}_{hh}\mathbf{T}_{hh} & \mathbf{R}_{hv}\mathbf{T}_{hh} & \mathbf{R}_{hh}\mathbf{T}_{vh} \\ \mathbf{R}_{vv}\mathbf{T}_{vh} & \mathbf{R}_{vh}\mathbf{T}_{hh} & \mathbf{R}_{vv}\mathbf{T}_{hh} & \mathbf{R}_{vh}\mathbf{T}_{vh} \\ \mathbf{R}_{hv}\mathbf{T}_{vv} & \mathbf{R}_{hh}\mathbf{T}_{hv} & \mathbf{R}_{hv}\mathbf{T}_{hv} & \mathbf{R}_{hh}\mathbf{T}_{vv} \end{bmatrix} \begin{bmatrix} \mathbf{S}_{vv}^t \\ \mathbf{S}_{hh}^t \\ \mathbf{S}_{vh}^t \\ \mathbf{S}_{hv}^t \end{bmatrix} + \begin{bmatrix} \mathbf{N}_{vv} \\ \mathbf{N}_{hh} \\ \mathbf{N}_{vh} \\ \mathbf{N}_{hv} \end{bmatrix}. \quad (4)$$

To simplify the numerical calculation, by absorbing all possible elements of  $\mathbf{R}_{ij}$  and  $\mathbf{T}_{ij}$  into one matrix  $m_{ij}$  without considering the noise contribution involving the scattering reciprocity theorem, (1) can be further expressed as follows:

$$\mathbf{S}^m = \mathbf{M}\mathbf{S}^t \quad (5)$$

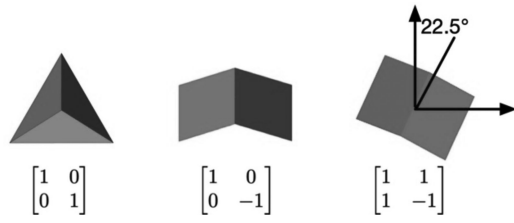
where

$$\mathbf{M} = \begin{bmatrix} m_{11} & m_{12} & m_{13} & m_{14} \\ m_{21} & m_{22} & m_{23} & m_{24} \\ m_{31} & m_{32} & m_{33} & m_{34} \\ m_{41} & m_{42} & m_{43} & m_{44} \end{bmatrix}. \quad (6)$$

The matrix  $\mathbf{M}$ , which is termed the calibration matrix, contains all distortions in the transmitter and receiver of the polarimetric SAR system. Using eight  $m$  matrices, with eight unknowns ( $m_{11}, m_{22}, m_{31}, m_{41}, m_{32}, m_{42}, m_{33}, m_{44}$ ) we can solve them and we obtain

$$\begin{bmatrix} \mathbf{S}_{vv}^m \\ \mathbf{S}_{hh}^m \\ \mathbf{S}_{vh}^m \\ \mathbf{S}_{hv}^m \end{bmatrix} = \begin{bmatrix} m_{11} & \frac{m_{32}m_{42}}{m_{22}} & \frac{m_{33}m_{42}}{m_{22}} & \frac{m_{32}m_{11}}{m_{33}} \\ \frac{m_{31}m_{41}}{m_{11}} & m_{22} & \frac{m_{33}m_{41}}{m_{11}} & \frac{m_{31}m_{22}}{m_{33}} \\ m_{31} & m_{32} & m_{33} & \frac{m_{32}m_{31}}{m_{33}} \\ m_{41} & m_{42} & \frac{m_{42}m_{41}}{m_{22}} & m_{44} \end{bmatrix} \begin{bmatrix} \mathbf{S}_{vv}^t \\ \mathbf{S}_{hh}^t \\ \mathbf{S}_{vh}^t \\ \mathbf{S}_{hv}^t \end{bmatrix}. \quad (7)$$

TABLE I  
SELECTED CORNER REFLECTORS AND TYPICAL SCATTERING MATRICES



### B. Method

A total of eight complex unknowns in the calibration matrix related to the copolarizations and cross polarizations need to be solved. Therefore, at least two calibration targets, one for copolarization and one for cross polarization, are required, forming eight independent complex equations for eight unknowns. In viewing six unknowns for copolarization, and two unknowns for cross polarization, passive CRs are sufficient and allow for convenient tracking and identification of potential error sources in the entire wave propagation process. One trihedral and one dihedral CR constitute two equations in copolarization, and a 22.5°-rotated dihedral CR forms four equations in full polarization. Note that the rotation is about the radar incidence plane. The theoretical scattering matrices for the above-selected reflectors are listed in Table I.

Based on the theoretical scattering matrices of the reference targets, one trihedral and one dihedral CR are used to solve the six unknown matrices ( $m_{11}, m_{22}, m_{21}, m_{31}, m_{41}, m_{42}$ ) that are related to copolarization. The solutions are given in

$$\begin{aligned} m_{11} &= \frac{S_{vv}^{m1} - S_{vv}^{m2}}{2}, & m_{22} &= \frac{S_{hh}^{m1} + S_{hh}^{m2}}{2} \\ m_{31} &= \frac{S_{vh}^{m1} - S_{vh}^{m2}}{2}, & m_{32} &= \frac{S_{vh}^{m1} + S_{vh}^{m2}}{2} \\ m_{41} &= \frac{S_{hv}^{m1} - S_{hv}^{m2}}{2}, & m_{42} &= \frac{S_{hv}^{m1} + S_{hv}^{m2}}{2} \end{aligned} \quad (8)$$

where  $S_{qp}^{m1}$  ( $q, p = h, v$ ) represents the element of the measured scattering matrix of a trihedral CR, and similarly  $S_{qp}^{m2}$  denotes the element of the measured scattering matrix of a dihedral CR. One 22.5°-rotated dihedral is used to work out the two unknowns ( $m_{33}, m_{44}$ ) that are related to cross polarization. The solutions read

$$\begin{aligned} m_{33} &= \frac{(m_{31} - m_{32} + S_{vh}^{m3}) \pm \sqrt{(-m_{31} + m_{32} - S_{vh}^{m3})^2 - 4m_{32}m_{31}}}{2} \\ m_{44} &= \frac{(m_{41} - m_{42} + S_{hv}^{m3}) \pm \sqrt{(-m_{41} + m_{42} - S_{hv}^{m3})^2 - 4m_{42}m_{41}}}{2} \end{aligned} \quad (9)$$

where  $S_{qp}^{m3}$  denotes the element of the measured scattering matrix of a 22.5°-rotated CR. After the M matrix has been determined, the calibrated scattering matrix can, readily, be obtained from

$$\mathbf{S}^c = \mathbf{M}^{-1} \mathbf{S}^m. \quad (10)$$

In summary, the flowchart of the polarimetric calibration method is displayed in Fig. 2.

We employ three reference targets with known measured scattering matrices  $\mathbf{S}^{m1}$ ,  $\mathbf{S}^{m2}$ , and  $\mathbf{S}^{m3}$  for the polarimetric

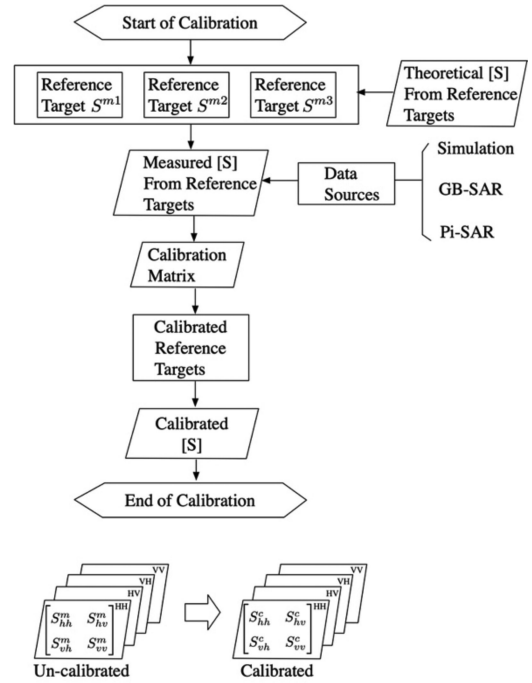


Fig. 2. Flowchart of the proposed polarimetric calibration method.

calibration. Based on the relation between the measured and the theoretical scattering matrices of the reference targets, we can obtain the desired calibration matrix. After the calibration matrix has been determined, the scattering matrices of the reference targets can, readily be, calibrated. It follows that the scattering matrices of unknown targets can be calibrated. The proposed method is validated with numerical simulation, the GB-SAR system, and airborne Pi-SAR data in the following sections.

To assess the accuracy of the proposed calibration technique, the calibrated amplitude and phase error is calculated according to

$$\tilde{A} = 20 \log_{10} \left( \frac{|\mathbf{S}^c|}{|\mathbf{S}^{\text{ref}}|} \right) \quad (11)$$

$$\tilde{\phi} = \arg(\mathbf{S}^c) - \arg(\mathbf{S}^{\text{ref}}) \quad (12)$$

where  $\mathbf{S}^c$  represents the calibrated scattering matrices of point targets, and  $\mathbf{S}^{\text{ref}}$  represents the theoretical scattering matrices of point targets.

## III. VALIDATION BY NUMERICAL SIMULATION

### A. Impact of Roll Angle for the 22.5°-Rotated Dihedral

In order to assess the impact of roll angle on the performance of the 22.5°-rotated dihedral CR, we plot the RCS responses for full polarization as a function of the elevation angle  $\theta$  and azimuth angle  $\phi$ , taking roll angle  $\phi$  from 0° to 90°, and  $\theta = 90^\circ$ ;  $\theta$  from 45° to 135°, and  $\phi = 0^\circ$ . Considering the impact of edge effects, a large-size (10 times wavelength) 22.5°-rotated dihedral CR ( $a = 2.36$  m) is simulated. The results, presented in Fig. 3(a) and (b), show that the polarized RCS patterns are quite close, with  $HV$  and  $VH$  being almost identical, confirming the theoretical responses. Note that the elevation angular pattern of

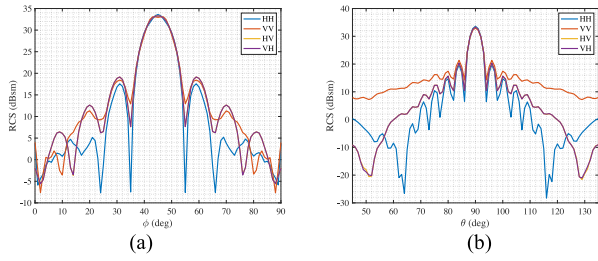


Fig. 3. RCS response of the  $22.5^\circ$ -rotated dihedral ( $a/\lambda \approx 10$ ) for full polarization along with (a) azimuth angle and (b) elevation angle. (*L*-band).

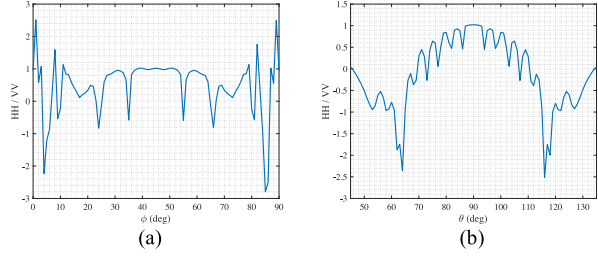


Fig. 4.  $HH/VV$  ratio of the  $22.5^\circ$ -rotated dihedral ( $a/\lambda \approx 10$ ) along with (a) azimuth angle and (b) elevation angle. (*L*-band).

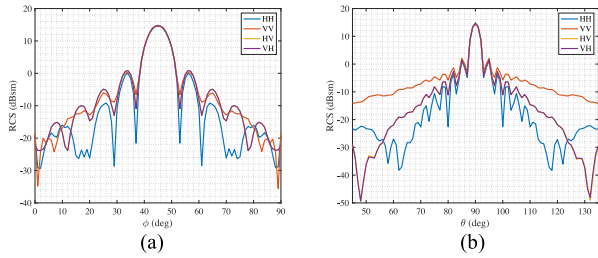


Fig. 5. RCS response of the  $22.5^\circ$ -rotated dihedral ( $a/\lambda \approx 10$ ) for full polarization along with (a) azimuth angle and (b) elevation angle. (*Ku*-band).

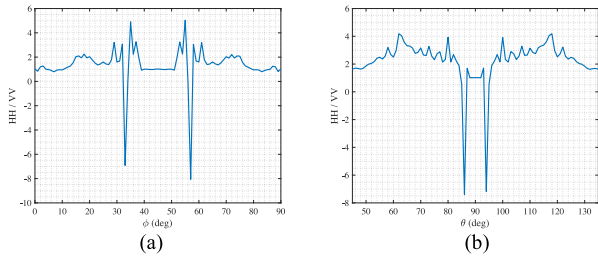
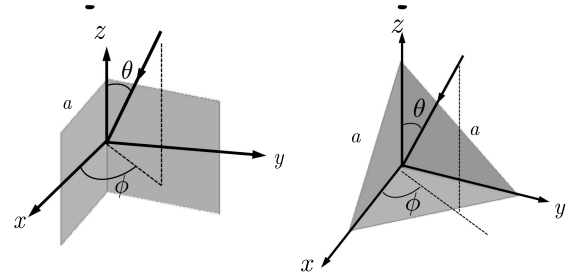


Fig. 6.  $HH/VV$  ratio of the  $22.5^\circ$ -rotated dihedral ( $a/\lambda \approx 10$ ) along with (a) azimuth angle and (b) elevation angle. (*Ku*-band).

$VV$  polarization deviates—at an acceptable level—from that of  $HH$  polarization for the higher order lobes.

For further evaluation, the  $HH/VV$  ratio results of the  $22.5^\circ$ -rotated dihedral (2.36 m) along with the rotation angle are plotted in Fig. 4(a) and (b). Between  $40^\circ$  and  $50^\circ$ , the  $HH/VV$  ratio fluctuates close to 1 as shown in Fig. 4(a), while in Fig. 4(b), a similar trend is observed between  $87^\circ$  and  $92^\circ$ .

A similar simulation is carried out at *Ku*-band. The side length of a  $22.5^\circ$ -rotated dihedral is set to 17 cm. The simulation results are shown in Figs. 5 and 6 and reveal that for an azimuth angle between  $40^\circ$  and  $50^\circ$ , the  $HH/VV$  ratio fluctuates approximately



	3dB Beamwidth (deg)	RCS (dBm <sup>2</sup> )
Trihedral	40	$4\pi a^4 / 3\lambda^2$
Dihedral	30	$8\pi a^4 / \lambda^2$
$22.5^\circ$ Dihedral	13	$4\pi a^4 / \lambda^2$

Fig. 7. Reference targets in numerical simulation.

to 1 in Fig. 6(a), while in Fig. 6(b) for an elevation angle between  $87^\circ$  and  $92^\circ$ , the  $HH/VV$  ratio approaches to 1.

By examining the angle sensitivity for a  $22.5^\circ$ -rotated dihedral, it is suggested that the elements of the scattering matrix are relatively sensitive to variations in azimuth and elevation angle. It is evident from Figs. 4 and 6 that the ranges of beamwidth, which corresponds to the theoretical scattering properties for the  $22.5^\circ$ -rotated dihedral, are about  $10^\circ$  in azimuth angle and  $5^\circ$  in elevation angle.

## B. Simulation

For the simulation, one trihedral, one dihedral, and one  $22.5^\circ$ -rotated dihedral CRs are considered, as shown in Fig. 7. The 3 dB beamwidth and maximum RCS (dBm<sup>2</sup>) are also shown, where  $a$  is the length of each side, and  $\lambda$  is the radar wavelength. As reference targets, their RCS for full polarizations are computed using method of moments (MoM) in FEKO simulations, with a length of about  $a = 2.36$  m and incidence angle of  $37^\circ$  at a radar wavelength of  $\lambda = 24$  cm (*L*-band,  $a/\lambda \approx 10$ ). To provide a reference for a GB-SAR system operating at *Ku*-band, a similar simulation is carried out with a length of about  $a = 17$  cm and at a radar wavelength of  $\lambda = 1.74$  cm (*Ku*-band,  $a/\lambda \approx 10$ ). Based on the relation between the measured and the theoretical scattering matrices of the reference targets, the calibration matrix can be solved, and the scattering matrices of the reference targets can be calibrated.

Concerning error analysis, Table II provides amplitude and phase errors for selected reference targets. Because the polarimetric calibration is primarily concerned with the channel imbalance and the cross-talk between transmitter and receiver, it is preferable to normalize the quantity with respect to a reference channel,  $HH$ -polarization or  $HV$ -polarization, whichever is applicable. For short notation, we denote trihedral and dihedral as Tr and Di, respectively, in Table II. As the amplitude and the phase errors for both *L*-band and *Ku*-band are within 0.1 dB and  $1^\circ$ , respectively.

TABLE II  
AMPLITUDE AND PHASE ERROR BEFORE AND AFTER CALIBRATION

	Before Calibration	After Calibration	Amplitude error (dB)	Phase error ( $^{\circ}$ )
<b>L-band</b>				
Tr-VV	$1.00 \angle 179.99^{\circ}$	$1 \angle 0^{\circ}$	0	0
Di-VV	$0.97 \angle 2.13^{\circ}$	$1 \angle 180^{\circ}$	0	0
22.5 $^{\circ}$ Di-VV	$0.96 \angle 3.05^{\circ}$	$0.99 \angle 179.11^{\circ}$	0.08	0.89
22.5 $^{\circ}$ Di-VH	$0.98 \angle 1.49^{\circ}$	$1 \angle 0^{\circ}$	0	0
22.5 $^{\circ}$ Di-HV	$0.98 \angle 178.50^{\circ}$	$1 \angle 0^{\circ}$	0	0
<b>Ku-band</b>				
Tr-VV	$1.00 \angle 179.99^{\circ}$	$1 \angle 0^{\circ}$	0	0
Di-VV	$0.97 \angle 2.13^{\circ}$	$1 \angle 180^{\circ}$	0	0
22.5 $^{\circ}$ Di-VV	$0.96 \angle 3.04^{\circ}$	$0.99 \angle 179.11^{\circ}$	0.08	0.89
22.5 $^{\circ}$ Di-VH	$0.98 \angle 1.48^{\circ}$	$1 \angle 0^{\circ}$	0	0
22.5 $^{\circ}$ Di-HV	$0.98 \angle 178.50^{\circ}$	$1 \angle 0^{\circ}$	0	0

#### IV. VALIDATION USING A GB-SAR SYSTEM

In this section, we conducted polarimetric calibration of a GB-SAR system using the hybrid CRs deployed in the field, to evaluate the polarimetric performance of the GB-SAR system from the beat signal of a trihedral CR before and after calibration.

##### A. Experiment Setup

An FMCW GB-SAR system operates at *Ku*-band with 300 MHz of bandwidth and 2 m of synthetic aperture length. The schematic illustration of the experiment, including the layout, positions and sizes of the CRs, is shown in Fig. 8; one trihedral and two dihedral CRs rotated at  $0^{\circ}$  and  $22.5^{\circ}$  were deployed in the open area. The side length of the targets was 20 cm and the target range was 20 m; the three targets were spaced approximately 5 m apart. Absorbing materials were used to reduce the unwanted reflections from the target stand and the ground.

##### B. SAR Images and Calibration Results

The SAR images were focused using the time-domain back-projection algorithm. The obtained fully PolSAR images of the illuminated area that were obtained are shown in Fig. 9. The three calibration targets are clearly identified in the copolarimetric images, whereas the  $22.5^{\circ}$ -rotated dihedral CR is observed in the full polarimetric images, as expected, which indicates that the deployment of the calibration targets was properly arranged. Then, the measured scattering matrices of the calibration targets were extracted from the PolSAR images, followed by a polarimetric calibration.

The calibrated results are given in Table III. It is seen that an amplitude error as low as 0.5 dB and a phase error within  $3^{\circ}$

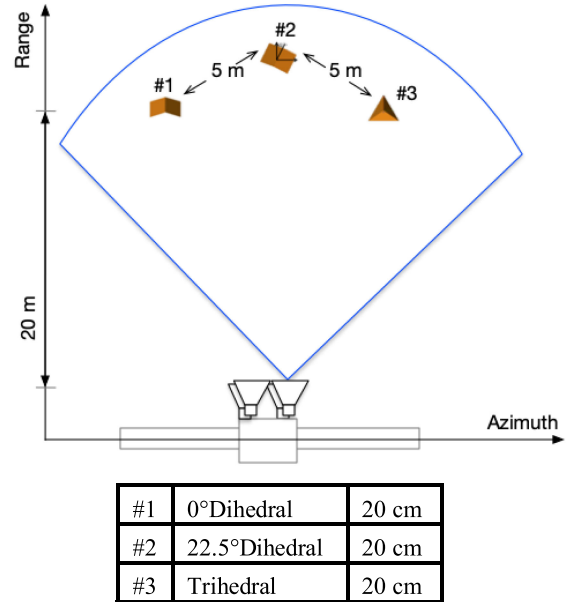


Fig. 8. Schematic illustration of the experiment and the layout, positions, and sizes of corner reflectors.

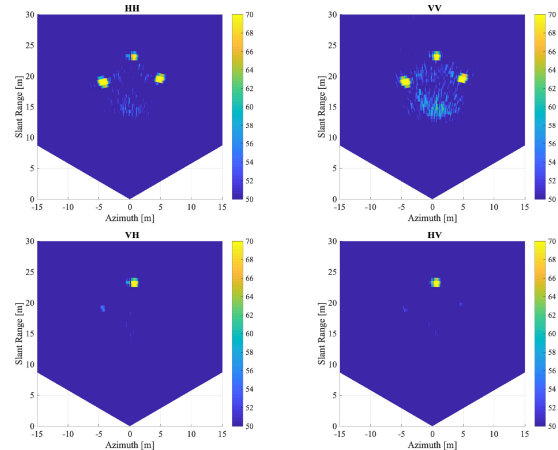


Fig. 9. Fully PolSAR images.

are attainable for a *Ku*-band GB-SAR system after the proposed polarimetric calibration.

##### C. Polarimetric Performance Evaluation

We now evaluate the polarimetric performance of the GB-SAR system before and after calibration by using an undertest trihedral CR with a side length of 20 m. The target range from the SAR was 20 m with the same layout as in Fig. 8, except the CRs were replaced by the undertest trihedral CR. We used the beat signal and took the HH as a reference channel to normalize the polarimetric responses, as presented in Fig. 10. Note that the amplitudes of the copolarization responses fluctuated within 5 dB, while the phase difference is approximately  $120^{\circ}$  between copolarizations before calibration, indicating severe crosstalk and channel imbalance between the transmitter and the receiver. After calibration, it can be seen that the phase of VV polarization for the trihedral CR is calibrated back to around  $0^{\circ}$ , as it should

TABLE III  
AMPLITUDE AND PHASE ERROR BEFORE AND AFTER CALIBRATION

	Before Calibration	After Calibration	Amplitude error (dB)	Phase error (°)
Tr-VV	1.14 $\angle$ 125.94°	1 $\angle$ 0°	0	0
0°Di-VV	1.12 $\angle$ 63.55°	1 $\angle$ 180°	0	0
22.5°Di-VV	1.42 $\angle$ 62.56°	1.05 $\angle$ 177.83°	0.42	2.17
22.5°Di-VH	1.78 $\angle$ 50.27°	1 $\angle$ 0.27°	0	0.27
22.5°Di-HV	1.47 $\angle$ 166.78°	1 $\angle$ 0.54°	0	0.54

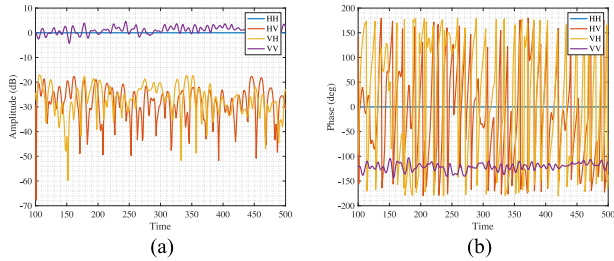


Fig. 10. Normalized polarimetric responses of a trihedral corner reflector before calibration.

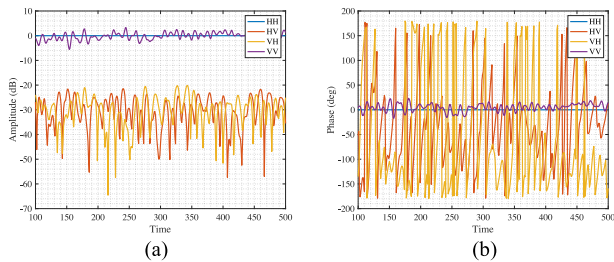


Fig. 11. Normalized polarimetric responses of a trihedral corner reflector after calibration.

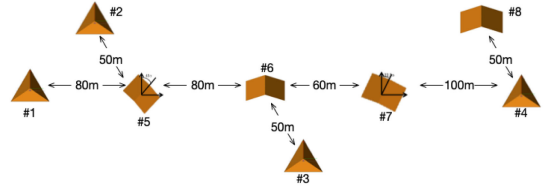
be (see Fig. 11). This confirms the effectiveness of the calibration method as developed in this study.

## V. VALIDATION USING PI-SAR SYSTEM

In this section, the proposed calibration is applied to an airborne *L*-band Pi-SAR data [23]. We further evaluate the effectiveness of the proposed method in two ways. First, we compare samples of polarimetric responses at selected CRs before and after calibration. Second, we perform intercomparisons of the RGB images before and after calibration on Pauli decomposition, Yamaguchi four-component decomposition, and TSVM decomposition.

### A. Data Description

The *L*-band Pi-SAR is an airborne high-resolution imaging radar system [23]. It was flown over the calibration site at Tottoridune on October 4, 2000, where eight CRs has been deployed for polarimetric calibration purpose [23]. The incidence angle was 53°. Eight CRs were deployed on the sandy area: four trihedral CRs, two dihedral CRs, one 45°-rotated dihedral and



#1-#4	Trihedral	80 cm
#5	45°Dihedral	80 cm
#6	0°Dihedral	80 cm
#7	22.5°Dihedral	60 cm
#8	0°Dihedral	60 cm

Fig. 12. Layout, position, and size of corner reflectors.

TABLE IV  
MEASURED SCATTERING MATRICES OF CORNER REFLECTORS

	HH	VV	HV	VH
Tr1	1 $\angle$ 0°	0.66 $\angle$ 7.03°	0.06 $\angle$ 98.32°	0.04 $\angle$ 98.27°
Tr2	1 $\angle$ 0°	0.65 $\angle$ 4.29°	0.04 $\angle$ 88.59°	0.04 $\angle$ 160.72°
Tr3	1 $\angle$ 0°	0.63 $\angle$ 13.53°	0.06 $\angle$ 96.11°	0.05 $\angle$ 107.36°
Tr4	1 $\angle$ 0°	0.67 $\angle$ 1.85°	0.05 $\angle$ 113.28°	0.07 $\angle$ 121.82°
Dr1	1 $\angle$ 0°	0.54 $\angle$ 183.56°	0.03 $\angle$ 97.32°	0.03 $\angle$ 87.22°
Dr2	1 $\angle$ 0°	0.49 $\angle$ 188.37°	0.03 $\angle$ 348.06°	0.06 $\angle$ 276.12°
22.5°Dr	1 $\angle$ 0°	0.61 $\angle$ 211.21°	0.78 $\angle$ 181.19°	0.86 $\angle$ 203.82°
45°Dr	0.16 $\angle$ 189.99°	0.04 $\angle$ 139.26°	1 $\angle$ 0°	0.93 $\angle$ 27.59°

TABLE V  
AMPLITUDE AND PHASE ERROR BEFORE AND AFTER CALIBRATION

	Before Calibration	After Calibration	Amplitude error (dB)	Phase error (°)
45°-Di VH	0.93 $\angle$ 27.59°	0.98 $\angle$ 2.14°	0.17	2.14

22.5°-rotated dihedral CR. The layout, positions, and sizes of these CRs are shown in Fig. 12.

### B. Error analysis

The measured scattering matrices of the eight CRs are extracted from the PolSAR image and presented in Table IV. We selected one trihedral, one dihedral, and one 22.5°-rotated dihedral CR as calibration targets, and the 45°-rotated dihedral CR was used to assess the effectiveness of the calibration. Applying the calibration technique, Table V provides the amplitude and phase error for the undertest target, which are satisfactorily acceptable.

### C. Polarimetric Signature

A good validation of calibration quality is the polarimetric signature of the calibrator [24]–[26], which is a way of visualizing the target scattering properties. We compared the polarimetric signatures of the CRs before and after calibration,

choosing four types of CRs as typical samples, one trihedral CR and three dihedral CRs with the rotation angles of  $0^\circ$ ,  $22.5^\circ$ , and  $45^\circ$ . These are shown in Fig. 13, in which the left column and right column, respectively, display the before and after-calibration polarimetric signatures of the CRs. We see that before calibration the polarimetric signatures show a noticeable distortion; while after calibration, the polarimetric signatures are much recovered and correspond with the theoretical values. It follows that the results confirm the reliability of the proposed calibration method. The results also suggest that the Pi-SAR image calibrated using the proposed method offers a high quality of polarimetric information.

#### D. Effect of Calibration on Pauli Decomposition

The objective of the Pauli decomposition [1] is to decompose the measured scattering matrix into four components corresponding to different scattering mechanisms, which are associated with each basis matrix, taking the forms

$$\mathbf{S} = \begin{bmatrix} S_{HH} & S_{HV} \\ S_{VH} & S_{VV} \end{bmatrix} = \frac{a}{\sqrt{2}} \begin{bmatrix} 1 & 0 \\ 0 & 1 \end{bmatrix} + \frac{b}{\sqrt{2}} \begin{bmatrix} 1 & 0 \\ 0 & -1 \end{bmatrix} + \frac{c}{\sqrt{2}} \begin{bmatrix} 0 & 1 \\ 1 & 0 \end{bmatrix} + \frac{d}{\sqrt{2}} \begin{bmatrix} 0 & -j \\ j & 0 \end{bmatrix} \quad (13)$$

where  $a, b, c,$  and  $d$  in (13) correspond to surface scattering, dihedral scattering, volume scattering and helix scattering, respectively, and are given by

$$a = \frac{S_{HH} + S_{VV}}{\sqrt{2}}, b = \frac{S_{HH} - S_{VV}}{\sqrt{2}}, c = \frac{S_{HV} + S_{VH}}{\sqrt{2}}, d = j \frac{S_{HV} - S_{VH}}{\sqrt{2}}. \quad (14)$$

A comparison of Pi-SAR data in Pauli decomposition before and after calibration is shown in Fig. 14, where the red rectangular box denotes the area in which the calibration targets were deployed.

To further examine the performance of the proposed calibration method, a detailed comparison of all reference targets is displayed in Fig. 15, where the term  $|HH+VV|$  represents the surface scattering,  $|HH-VV|$  the dihedral scattering, and  $HV$  the volume scattering. Consequently, an RGB image can be composed with the intensities  $|a|^2$ ,  $|b|^2$ , and  $|c|^2$ , which, as illustrated before, correspond to distinct physical scattering mechanisms. According to a theoretical scattering matrix, the trihedral in  $|HH+VV|$  is maximum and the rest are zero, ideally. Therefore, the color-coded targets in the image should be in blue, and the three dished at  $0^\circ$ ,  $22.5^\circ$ , and  $45^\circ$  rotation should be in red, yellow, and green, respectively. As shown in Fig. 15, the purple target within the circle is the trihedral CR, while the pink target within the triangle is the dihedral CR. Before calibration, the trihedral is in purple and the dihedral is in pink in the image, which represents certain degrees of cross-talk contamination and channel imbalance. After calibration, the trihedral corrects to blue and the dihedral to red, as both are accurately recovered.

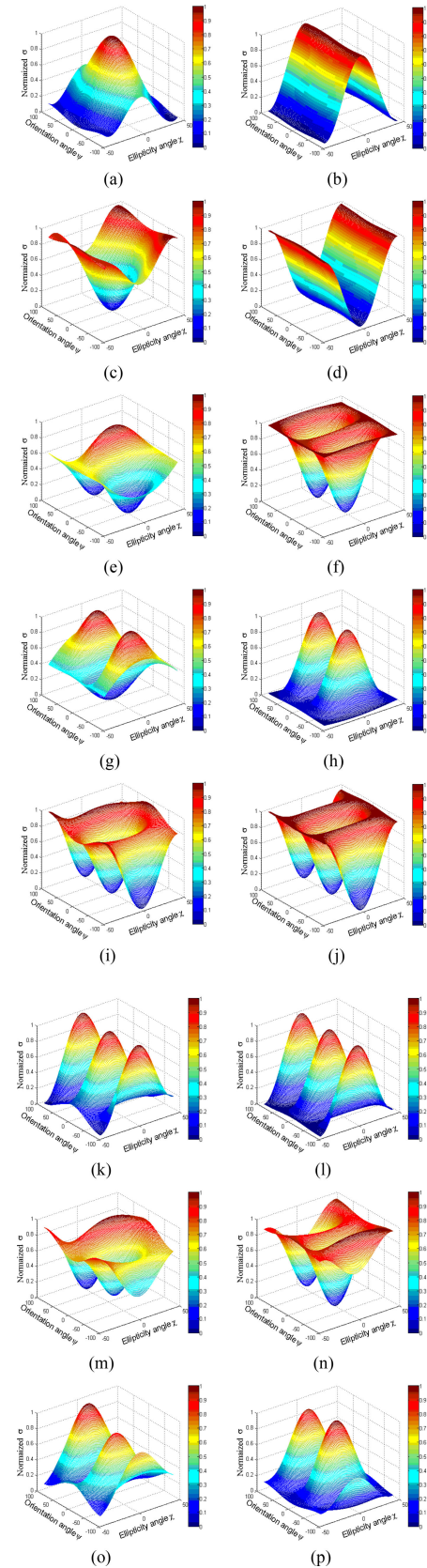


Fig. 13. Polarimetric signatures of the four corner reflectors in uncalibrated and calibrated data. (a), (b) Copol signature of Tr. (c), (d) Cross-pol signature of Tr. (e), (f) Copol signature of Dr. (g), (h) Cross-pol signature of Dr. (i), (j) Copol signature of  $45^\circ$ Dr. (k), (l) Cross-pol signature of  $45^\circ$ Dr. (m), (n) Copol signature of  $22.5^\circ$ Dr. (o), (p) Cross-pol signature of  $22.5^\circ$ Dr.

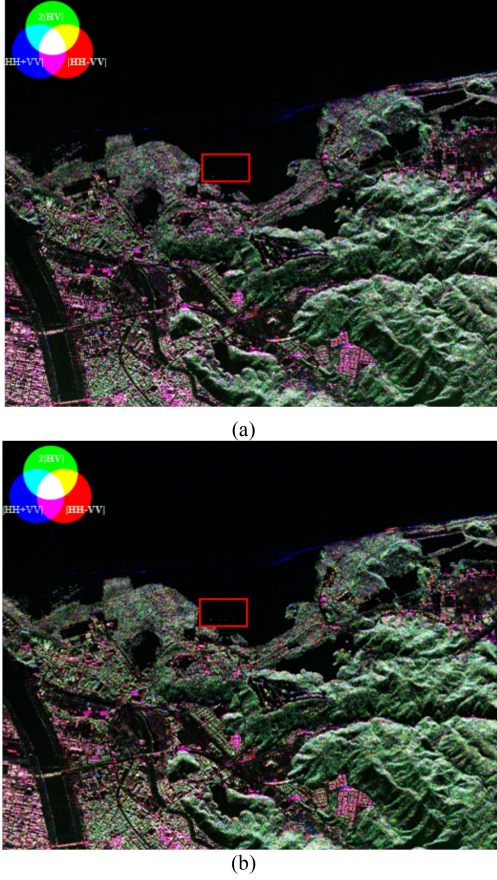


Fig. 14. Comparison of Pi-SAR data in Pauli decomposition (a) before calibration and (b) after calibration.

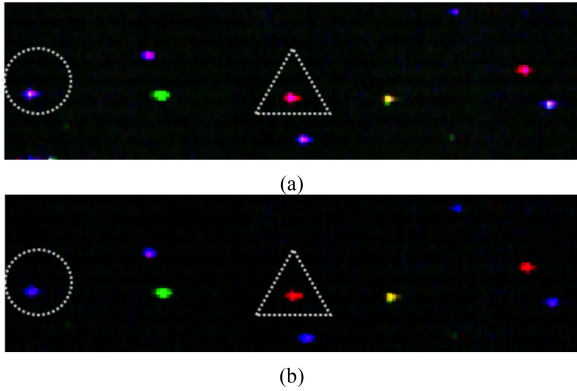


Fig. 15. Detailed comparison of Pi-SAR data in Pauli decomposition (a) before calibration and (b) after calibration.

### E. Effect of Calibration on Yamaguchi Decomposition

Polarimetric calibration is a critical procedure for correct and accurate target decomposition. Hence, it is constructive to process the Pi-SAR data with a Yamaguchi four-component decomposition scheme [28] as an illustrative example. The measured coherency matrix  $\langle[\mathbf{T}_y]\rangle$  is decomposed into four independent components, i.e., surface scattering, dihedral scattering, volume scattering, and helix scattering, to verify the inherent

polarimetric characteristics of the reference targets

$$\begin{aligned} \langle[\mathbf{T}_y]\rangle &= f_s \langle[\mathbf{T}_y]\rangle_{\text{surface}} + f_d \langle[\mathbf{T}_y]\rangle_{\text{dihedral}} \\ &\quad + f_v \langle[\mathbf{T}_y]\rangle_{\text{volume}} + f_h \langle[\mathbf{T}_y]\rangle_{\text{helix}} \end{aligned} \quad (15)$$

where  $f_s, f_d, f_v$ , and  $f_h$  are the coefficients associated with each component, to be determined,  $\langle[\mathbf{T}_y]\rangle_{\text{surface}}$ ,  $\langle[\mathbf{T}_y]\rangle_{\text{dihedral}}$ ,  $\langle[\mathbf{T}_y]\rangle_{\text{volume}}$ , and  $\langle[\mathbf{T}_y]\rangle_{\text{helix}}$  are expansion matrices corresponding to the surface, dihedral, volume, and helix scattering, respectively.

It is known that oriented urban and vegetation characteristics are decomposed into the volume scattering mechanism and it is difficult to discriminate the vegetation from oblique urban areas. Huynen [27] first proposed a deorientation method to resolve this problem. The coherency matrix after rotation by angle  $\theta$  can be obtained by

$$[\mathbf{T}'_y] = [\mathbf{R}_y(\theta)] [\mathbf{T}_y] [\mathbf{R}_y(\theta)]^T \quad (16)$$

where  $\mathbf{T}$  denotes the conjugate transpose, and

$$[\mathbf{R}_y(\theta)] = \begin{bmatrix} 1 & 0 & 0 \\ 0 & \cos 2\theta & \sin 2\theta \\ 0 & -\sin 2\theta & \cos 2\theta \end{bmatrix}. \quad (17)$$

The surface scattering is given by

$$\langle[\mathbf{T}'_y]\rangle_{\text{surface}} = \begin{bmatrix} 1 & \beta^* & 0 \\ \beta & |\beta|^2 & 0 \\ 0 & 0 & 0 \end{bmatrix}, |\beta| < 1. \quad (18)$$

The dihedral scattering is

$$\langle[\mathbf{T}'_y]\rangle_{\text{dihedral}} = \begin{bmatrix} |\alpha|^2 & \alpha & 0 \\ \alpha^* & 1 & 0 \\ 0 & 0 & 0 \end{bmatrix}, |\alpha| < 1 \quad (19)$$

where the coefficients  $\alpha$  and  $\beta$  are to be determined.

The helix scattering is of the form

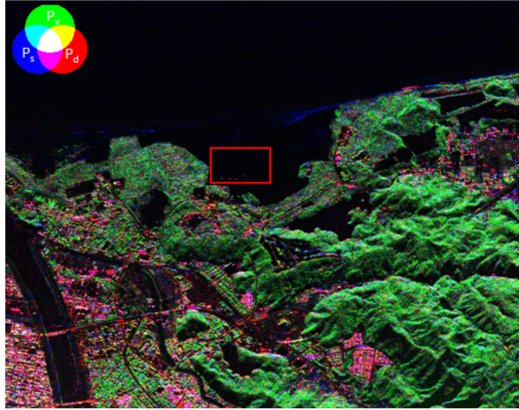
$$\langle[\mathbf{T}'_y]\rangle_{\text{helix}} = \frac{1}{2} \begin{bmatrix} 0 & 0 & 0 \\ 0 & 1 & \pm j \\ 0 & \mp j & 1 \end{bmatrix}. \quad (20)$$

For the volume scattering, one of the following matrices is adopted subject to conditions

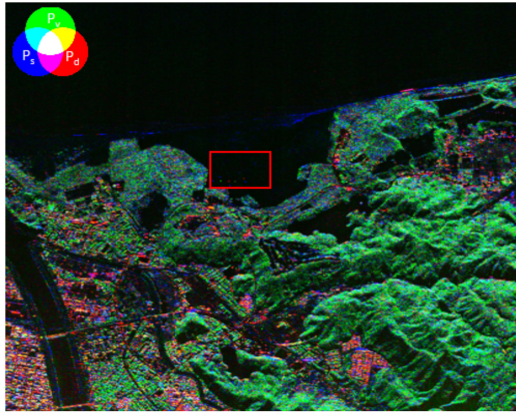
$$\begin{aligned} \langle[\mathbf{T}'_y]\rangle_{\text{volume}} &= \frac{1}{30} \begin{bmatrix} 15 & 5 & 0 \\ 5 & 7 & 0 \\ 0 & 0 & 8 \end{bmatrix} \quad (21) \\ \text{if } 10 \log \left( \frac{\langle|S_{VV}|^2\rangle}{\langle|S_{HH}|^2\rangle} \right) &< -2\text{dB} \end{aligned}$$

$$\begin{aligned} \langle[\mathbf{T}'_y]\rangle_{\text{volume}} &= \frac{1}{4} \begin{bmatrix} 2 & 0 & 0 \\ 0 & 1 & 0 \\ 0 & 0 & 1 \end{bmatrix} \quad (22) \\ \text{if } 10 \log \left( \frac{\langle|S_{VV}|^2\rangle}{\langle|S_{HH}|^2\rangle} \right) &< 2\text{dB} \end{aligned}$$





(a)



(b)

Fig. 16. Comparison of Pi-SAR data in Yamaguchi decomposition (a) before calibration and (b) after calibration.

$$\langle [\mathbf{T}'_{\mathbf{y}}] \rangle_{\text{volume}} = \frac{1}{30} \begin{bmatrix} 15 & -5 & 0 \\ -5 & 7 & 0 \\ 0 & 0 & 8 \end{bmatrix} \quad (23)$$

if  $10 \log \left( \frac{\langle |S_{VV}|^2 \rangle}{\langle |S_{HH}|^2 \rangle} \right) > 2\text{dB}$ .

For the case of  $10 \log(\langle |S_{VV}|^2 \rangle / \langle |S_{HH}|^2 \rangle) < 2\text{dB}$ , the power for each component becomes

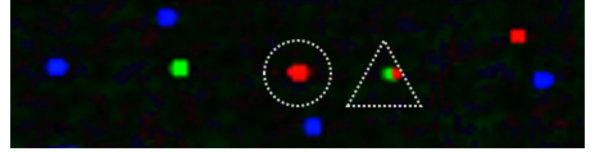
$$\begin{aligned} P_h &= f_h = 2 |Im \langle S_{HV}^* (S_{HH} - S_{VV}) \rangle| \\ P_v &= f_v = 8 \langle |S_{HV}|^2 \rangle - 2P_h \\ P_s &= f_s = (1 + |\beta|^2) \\ P_d &= f_d = (1 + |\alpha|^2) \end{aligned} \quad (24)$$

where  $\mathcal{I}m$  denotes the imaginary part in a complex variable.

Fig. 16 displays the before and after calibration comparison of the Yamaguchi four-component decomposition with color-coded: dihedral (red), surface (blue), and volume scattering (green). Visually, the after-calibration image is less reddish than the before-calibration one. The difference indicates that the “red” caused by dihedral scattering is weakened, while the “green” representing the volume scattering is enhanced. In urban area containing roads, trees and buildings, the dihedral scattering and volume scattering are fused. After calibration, different



(a)



(b)

Fig. 17. Detailed comparison of Yamaguchi decomposition (a) before calibration and (b) after calibration.

types of targets illustrate the colors correctly corresponding to the scattering mechanism.

To verify the enhancement of the decomposition more clearly, we enlarged the red rectangle area in Fig. 16 to present a detailed comparison of all the reference targets before and after calibration. The  $45^\circ$ -rotated dihedral CR is displayed inside the white circle, and the  $22.5^\circ$ -rotated dihedral CR is presented inside the white triangle. From the theoretical scattering matrix, the  $45^\circ$ -rotated dihedral CR can only produce cross-polarization scattering power. This contributes to volume scattering in Yamaguchi four-component decomposition, while the  $22.5^\circ$ -rotated dihedral CR provides equal power of the copolarization and cross-polarization scattering. Hence, the dihedral at  $45^\circ$  rotation should be in red, and the dihedral at  $22.5^\circ$  rotation should be in a combination of red and green. Before calibration, the dihedrals at the  $45^\circ$  and  $22.5^\circ$  rotation are both in pink in Fig. 17(a), indicating that there are distortions between channels. After calibration, the  $45^\circ$ -rotated dihedral is now in red, as shown in the white circle in Fig. 17(b), and the  $22.5^\circ$ -rotated dihedral is both green and red, as shown in the white triangle in Fig. 17(b). At this point, all the reference targets show the correct polarimetric scattering properties as they should be. The results confirm that the removal of cross-talk and channel imbalance is satisfactory.

#### F. Effect of Calibration on TSVM Decomposition

In this section, we show the influence of calibration on the polarization parameters derived from TSVM decomposition [29], [30]. Three target parameters,  $\alpha_s$ ,  $\Phi_{\alpha_s}$ , and  $\tau_m$ , are selected for analysis. For an unambiguous description of target scattering type,  $\alpha_s$  and  $\Phi_{\alpha_s}$  are referred to as the symmetric scattering type magnitude and phase respectively, denoted by (25). The term  $\tau_m$  is used to evaluate target symmetry; a symmetric target has zero helicity, i.e.,  $\tau_m = 0$

$$\tan(\alpha_s) e^{j\Phi_{\alpha_s}} = \frac{\lambda_1 - \lambda_2}{\lambda_1 + \lambda_2} \quad (25)$$

where  $\lambda_1$  and  $\lambda_2$  are the two complex con-eigenvalues of the scattering matrix.  $\alpha_s$  is defined in the interval  $0 \leq \alpha_s \leq \pi/2$ , and leads to  $-\pi/2 \leq \Phi_{\alpha_s} \leq \pi/2$ .

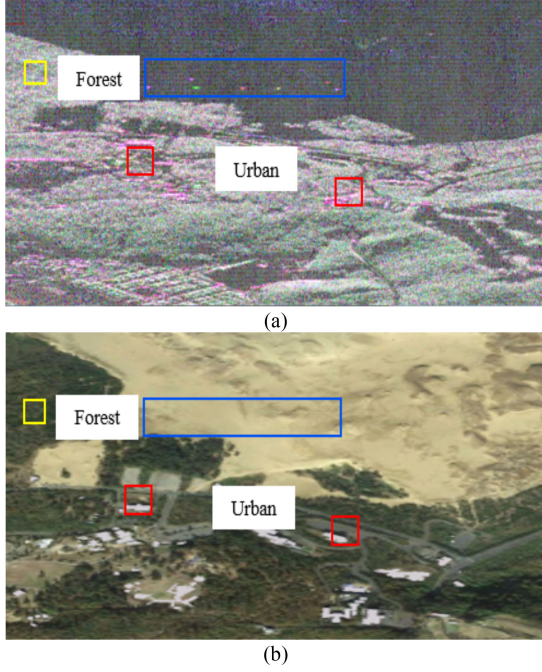


Fig. 18. Polarmetric Pi-SAR (a) Pauli RGB image and (b) corresponding aerial image from Google Earth.

The scattering vector can be given as a function of target helicity  $\tau_m$  and con-eigenvalues  $\lambda_1$  and  $\lambda_2$  by

$$\begin{aligned} \vec{e}_T^{SV} &= a_m |\vec{e}_T|_m \cdot \exp^{j\Phi_s} \begin{bmatrix} 1 & 0 & 0 \\ 0 & \cos 2\psi & -\sin 2\psi \\ 0 & \sin 2\psi & \cos 2\psi \end{bmatrix} \\ &\times \begin{bmatrix} \cos \alpha_s \cos 2\tau_m \\ \sin \alpha_s e^{j\Phi_{\alpha_s}} \\ -j \cos \alpha_s \sin 2\tau_m \end{bmatrix} \end{aligned} \quad (26)$$

where  $|\vec{e}_T|_m = \vec{e}_T^{SV} / a_m$ , and  $a_m$  is the maximum amplitude return,  $\Phi_s$  can be ignored for noninterferometric applications, and  $\psi$  is defined as the target orientation along the radar line of sight. Because we emphasize the inherent properties of the scatter targets, it is necessary to apply the deorientation.

Rotating the scattering vector  $\vec{e}_T^{SV}$  about the line of sight by an angle  $-\psi$  [31] leads to the roll-invariant target vector

$$\vec{V}^{\text{roll-inv}} = a_m \begin{bmatrix} \cos \alpha_s \cos 2\tau_m \\ \sin \alpha_s e^{j\Phi_{\alpha_s}} \\ -j \cos \alpha_s \sin 2\tau_m \end{bmatrix}. \quad (27)$$

The RGB polarimetric Pi-SAR Pauli image and the corresponding aerial image from Google Earth are shown in Fig. 18; the scene included forests and buildings. In Fig. 18, the red boxes denote small buildings chosen for analysis, for an urban area is selected as predominantly dihedral scattering, and the blue rectangle indicates the calibration site containing eight CRs.

From the perspective of the calibration target, the color should be red in an ideal situation, where the  $\alpha_s$  angle of the circled CR is projected onto the Pauli basis. As shown in Fig. 19(a), the dihedral CR changes to orange before calibration; the response

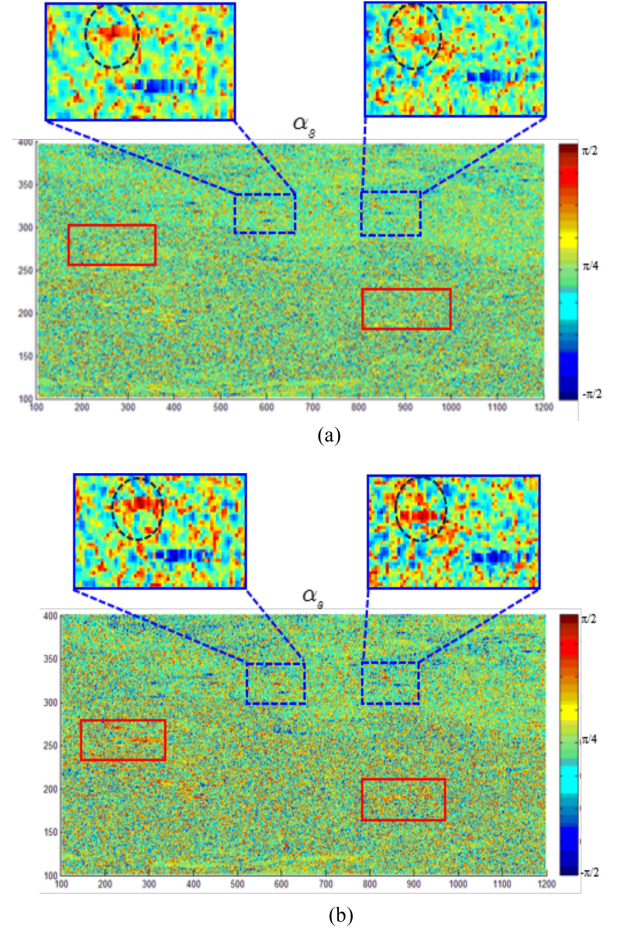


Fig. 19. Comparison of  $\alpha_s$  angles (a) before calibration and (b) after calibration.

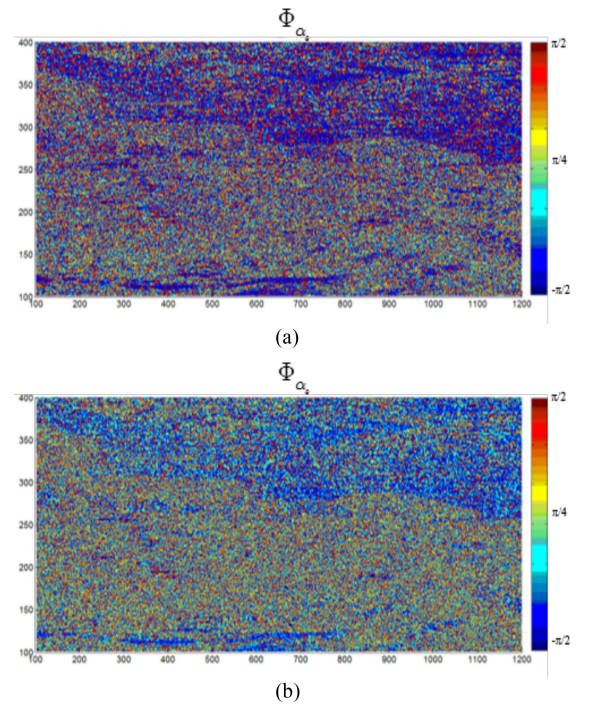


Fig. 20. Comparison of  $\Phi_{\alpha_s}$  angles (a) before calibration and (b) after calibration.

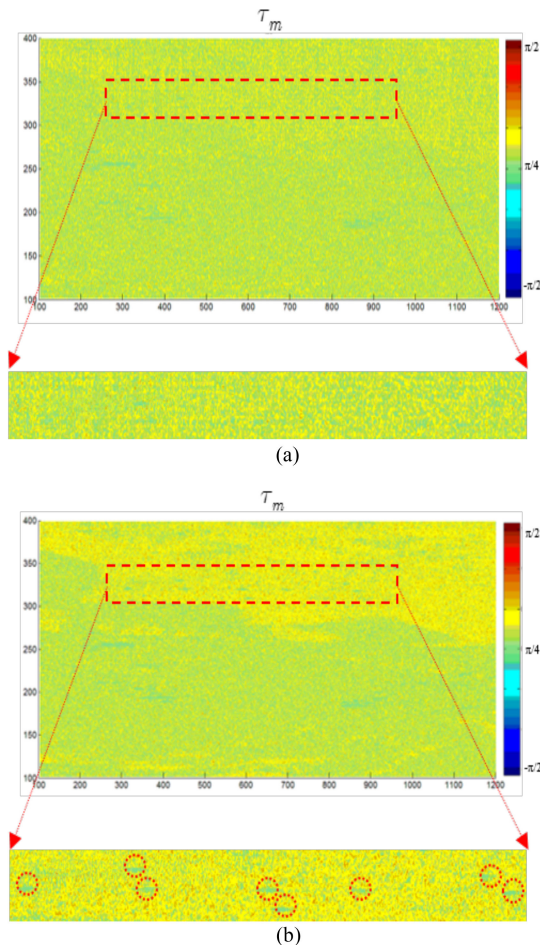


Fig. 21. Comparison of  $\tau_m$  angles (a) before calibration and (b) after calibration.

changes to red after calibration [see Fig. 19(b)]. In the image, the buildings are classified as dominated by dihedral scattering. Compared to before calibration, after calibration the red color representing the building is now correctly recovered [see the red box in Fig. 19(b)]. The abovementioned results come to confirm the effectiveness of the proposed calibration approach.

To evaluate the impact of calibration on the helicity angle, a comparison of helicity angles before and after calibration is performed, as shown in Fig. 20. Target helicity angle indicates the symmetric-nonsymmetric nature of the scattering target. In practice, the helicity-related portion of polarimetric information is often small in magnitude. However, in the most general case, targets may be either symmetric or asymmetric. As shown in the rectangle box area of Fig. 21, the reflector array from the before-calibration image was not identical; however, it became identical after calibration. This comparison provides a further validation of the proposed calibration technique.

## VI. CONCLUSION

In this article, we evaluated a polarimetric calibration method using hybrid CRs. The method requires only one trihedral and two dihedral CRs with different rotation angles. In the assessment, numerically simulated data, the GB-SAR system, and

airborne L-band Pi-SAR data were used. The results show that both cross-talk and channel imbalance are removed with a high degree of accuracy using the proposed method. The amplitude error can be confined within 0.5 dB, while the phase error is about  $3^\circ$  in both GB-SAR and Pi-SAR data. The impact of the roll angle for the  $22.5^\circ$ -rotated dihedral CR was analyzed via numerical simulation, indicating that the range of beamwidth is approximately  $10^\circ$  in azimuth angle and  $5^\circ$  in elevation angle. For the Pi-SAR data, the calibration fidelity was demonstrated by comparing the polarimetric signature responses of the selected CRs before and after calibration, proving that excellent agreement between the calibrated, and the theoretical polarimetric responses is keenly attainable. Accurate calibration is critical for target decomposition, as shown in Pauli decomposition and Yamaguchi four-component decomposition, and can be affected if the crosstalk and channel imbalance are not effectively taken out. From the perspective of polarimetric parameters, three target parameters, including  $\alpha_s$ ,  $\Phi_{\alpha_s}$ , and  $\tau_m$  derived from the TSVM decomposition, can be used as a measure of calibration quality. Before these target parameters can be consistently retrieved, polarimetric calibration, next to data acquiring, is essential.

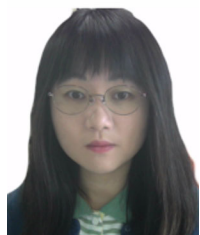
## ACKNOWLEDGMENT

The authors would like to thank Prof. Y. Yamaguchi from Niigata University - Japan for providing the Pi-SAR data.

## REFERENCES

- [1] J. S. Lee and E. Pottier, *Polarimetric Radar Imaging: From Basics to Applications*. Boca Raton, FL, USA: CRC Press, 2009.
- [2] S. R. Cloude, *Polarisation: Applications in Remote Sensing*. London, U.K.: Oxford Univ. Press, 2009.
- [3] A. Freeman, "SAR calibration: An overview," *IEEE Trans. Geosci. Remote Sens.*, vol. 30, no. 6, pp. 1107–1121, Nov. 1992.
- [4] J.-R. J. Gau and W. D. Burnside, "New polarimetric calibration technique using a single calibration dihedral," *Proc. Inst. Elect. Eng., Microw. Antennas Propag.*, vol. 142, no. 1, pp. 19–25, Feb. 1995.
- [5] M. W. Whitt, F. T. Ulaby, P. Polatin, and V. V. Liepa, "A general polarimetric radar calibration technique," *IEEE Trans. Antennas Propag.*, vol. 39, no. 1, pp. 62–67, Jan. 1991.
- [6] A. Freeman, J. J. Van Zyl, J. D. Klein, H. A. Zebker, and Y. Shen, "Calibration of stokes and scattering matrix format polarimetric SAR data," *IEEE Trans. Geosci. Remote Sens.*, vol. 30, no. 3, pp. 531–539, May 1992.
- [7] J. J. Van Zyl, "Calibration of polarimetric radar images using only image parameters and trihedral corner reflector responses," *IEEE Trans. Geosci. Remote Sens.*, vol. 28, no. 3, pp. 337–348, May 1990.
- [8] K. Sarabandi, F. T. Ulaby, and M. C. Dobson, "AIRSAR and POLARSCAT cross-calibration using point and distributed targets," *IEEE Trans. Geosci. Remote Sens.*, vol. 2, no. 4, pp. 18–21, Aug. 1993.
- [9] R. M. Barnes, "Polarimetric calibration using in-scene reflectors," in *Proc. MIT Lincoln Lab*, Lexington, MA, USA, Rep. TT-65, Sep. 1986.
- [10] M. Satake *et al.*, "Development of polarization selective corner reflectors and its experiment for calibration of airborne polarimetric synthetic aperture radar," in *Proc. IEEE Int. Geosci. Remote Sens. Symp.*, Jul. 2001, pp. 417–419.
- [11] A. Freeman, Y. Shen, and C. L. Werner, "Polarimetric SAR calibration experiment using active radar calibrators," *IEEE Trans. Geosci. Remote Sens.*, vol. 28, no. 2, pp. 224–240, Mar. 1990.
- [12] K. Sarabandi *et al.*, "Polarimetric calibration of SIR-C using point and distributed targets," *IEEE Trans. Geosci. Remote Sens.*, vol. 33, no. 4, pp. 858–866, Jul. 1995.
- [13] M. Fujita, T. Masuda, Y. Fujino, and M. Satake, "Polarimetric calibration of the SIR-C C-band channel using active radar calibrators and polarization selective dihedrals," *IEEE Trans. Geosci. Remote Sens.*, vol. 36, no. 6, pp. 1872–1878, Nov. 1998.

- [14] J. D. Klein, "Calibration of complex polarimetric SAR imagery using backscatter correlations," *IEEE Trans. Aerosp. Electron. Syst.*, vol. 28, no. 7, pp. 183–194, Jan. 1992.
- [15] K. Sarabandi, "Calibration of a polarimetric synthetic aperture radar using a known distributed target," *IEEE Trans. Geosci. Remote Sens.*, vol. 32, no. 3, pp. 575–583, May 1994.
- [16] S. Quegan, "A unified algorithm for phase and cross-talk calibration of polarimetric data-theory and observations," *IEEE Trans. Geosci. Remote Sens.*, vol. 32, no. 1, pp. 89–99, Jan. 1994.
- [17] K. Sarabandi, F. T. Ulaby, and M. A. Tassoudji, "Calibration of polarimetric radar systems with good polarization isolation," *IEEE Trans. Geosci. Remote Sens.*, vol. 28, no. 1, pp. 70–75, Jan. 1990.
- [18] S. H. Yueh, J. A. Kong, R. M. Barnes, and A. R. T. Shin, "Calibration of polarimetric radars using in-scene reflectors," *J. Electromagn. Waves Appl.*, vol. 4, no. 1, pp. 27–48, Apr. 1990.
- [19] M. Shimada, "Model-Based polarimetric SAR calibration method using forest and surface-scattering targets," *IEEE Trans. Geosci. Remote Sens.*, vol. 49, no. 5, pp. 1712–1733, May 2011.
- [20] R. Touzi and M. Shimada, "Polarimetric PALSAR calibration," *IEEE Trans. Geosci. Remote Sens.*, vol. 47, no. 12, pp. 3951–3959, Dec. 2009.
- [21] H. Kimura, "Calibration of polarimetric PALSAR imagery affected by faraday rotation using polarization orientation," *IEEE Trans. Geosci. Remote Sens.*, vol. 47, no. 12, pp. 3943–3950, Dec. 2009.
- [22] T. L. Ainsworth, L. Ferro-Famil, and J.-S. Lee, "Orientation angle preserving a posteriori polarimetric SAR calibration," *IEEE Trans. Geosci. Remote Sens.*, vol. 44, no. 4, pp. 994–1003, Apr. 2006.
- [23] M. Satake *et al.*, "Flight experiments of airborne high-resolution multi-Parameter imaging radar, Pi-SAR," *J. Commun. Res. Lab.*, vol. 49, no. 2, pp. 127–141, Jun. 2002.
- [24] S. L. Durden, J. J. Van Zyl, and H. A. Zebker, "Modeling and observation of the radar polarization signature of forested areas," *IEEE Trans. Geosci. Remote Sens.*, vol. 27, no. 3, pp. 290–301, May 1989.
- [25] H. A. Zebker, J. J. Van Zyl, and D. N. Held, "Imaging radar polarimetry from wave synthesis," *J. Geophys. Res.*, vol. 92, no. b1, pp. 683–701, Jan. 1987.
- [26] J. J. Van Zyl, H. A. Zebker, and C. Elachi, "Imaging radar polarization signatures - theory and observation," *Radio Sci.*, vol. 22, no. 4, pp. 529–543, Jul. 1987.
- [27] J. R. Huynen, "Phenomenological theory of radar targets," Ph.D. dissertation, Tech. Univ., Delft, The Netherlands, Dec. 1970.
- [28] Y. Yamaguchi, A. Sato, W. Boerner, R. Sato, and H. Yamada, "Four-Component scattering power decomposition with rotation of coherency matrix," *IEEE Trans. Geosci. Remote Sens.*, vol. 49, no. 6, pp. 2251–2258, Jun. 2011.
- [29] R. Touzi, "Target scattering decomposition in terms of roll-invariant target parameters," *IEEE Trans. Geosci. Remote Sens.*, vol. 45, no. 1, pp. 73–84, Jan. 2007.
- [30] R. Touzi, F. Charbonneau, R. K. Hawkins, and P. W. Vachon, "Ship detection and characterization using polarimetric SAR," *Can. J. Remote Sens.*, vol. 30, no. 3, pp. 552–559, 2004.
- [31] J. S. Lee, D. L. Shuler, and T. L. Ainsworth, "Polarimetric SAR data compensation for terrain azimuth slope variation," *IEEE Trans. Geosci. Remote Sens.*, vol. 38, no. 5, pp. 2153–2163, Sep. 2000.



**Suyun Wang** received the Ph.D. degree in environmental studies from the Tohoku University, Sendai, Japan, in 2020.

She is currently with the Center for Northeast Asian Studies, Tohoku University, as a research fellow. Her current research interests include development of ground-based synthetic aperture radar systems and algorithms, polarimetric radar calibration, polarimetric and interferometric SAR, and bistatic radar.



**Kun-Shan Chen** (Fellow, IEEE) received the Ph.D. degree in electrical engineering from the University of Texas at Arlington, Arlington, TX, USA, in 1990.

From 1992 to 2014, he was a Professor with the National Central University, Taiwan, was with the Institute of Remote Sensing and Digital Earth, Chinese Academy of Sciences, China from 2014 to 2019. Since 2019, he has been with Guilin University of Technology. He has authored and coauthored more than 170 refereed journal papers, contributed ten book chapters, coauthor (with A. K. Fung) of *Microwave Scattering and Emission Models for Users* (Artech House, 2010), author of *Principles of Synthetic Aperture Radar: A System Simulation Approach* (CRC Press, 2015), and coeditor (with X. Li, H. Guo, X. Yang) of *Advances in SAR Remote Sensing of Ocean* (CRC Press, FL, USA, 2018), and *Radar Scattering and Imaging of Rough Surface: Modeling and Applications with Matlab* (CRC Press, 2020). His research interests include microwave remote sensing theory, modeling, system, measurement, and intelligent signal processing and data analytics for radar.

Prof. Chen was a Guest Editor for the IEEE TRANSACTIONS ON GEOSCIENCE AND REMOTE SENSING Special Issue on Remote Sensing for Major Disaster Prevention, Monitoring, and Assessment (2007), Guest Editor for the *Proceedings of IEEE SPECIAL ISSUE ON REMOTE SENSING for Natural Disaster* (2012), IEEE GRSS Adcom member (2010–2014), a founding chair of the GRSS Taipei Chapter, an Associate Editor for the IEEE TRANSACTIONS ON GEOSCIENCE AND REMOTE SENSING, since 2000, as founding Deputy Editor-in-Chief of IEEE JOURNAL OF SELECTED TOPICS IN APPLIED EARTH OBSERVATIONS AND REMOTE SENSING (2008–2010). He was also a Guest Editor of the special issue of Data Restoration and Denoising of Remote Sensing Data, and special issues of Radar Imaging Theory, Techniques, and Applications, both for *Remote Sensing*, and was Co-Chair of Technical Committee for IGARSS 2016 and IGARSS2017. He was a member of the editorial board of the Proceedings of IEEE (2014–2019) and has been a member of the editorial board of the IEEE ACCESS since 2020.



**Motoyuki Sato** (Fellow, IEEE) received the B.E., M.E., and Dr. Eng. degrees in information engineering from Tohoku University, Sendai, Japan, in 1980, 1982, and 1985, respectively.

Since 1997, he has been a Professor with Tohoku University and a Distinguished Professor of Tohoku University 2007–2011, the Director of Center for Northeast Asian Studies, Tohoku University 2009–2013. He was a Visiting Researcher with the Federal German Institute for Geoscience and Natural Resources (BGR), Hannover, Germany, in 1988–1989.

He was a visiting Professor at Jilin University, China, Delft University of Technology, The Netherlands, and Mongolian University of Science and Technology. His current interests include transient electromagnetics and antennas, radar polarimetry, ground penetrating radar (GPR), borehole radar, electromagnetic induction sensing, GB-SAR, and MIMO radar systems.

Dr. Sato developed GPR sensors for humanitarian demining, and they are used in mine affected countries including Cambodia. He was the recipient of 2014 Frank Frischknecht Leadership Award from SEG for his contribution to his sustained and important contributions to near-surface geophysics in the field of ground-penetrating radar. He received IEICE Best Paper Award (Kiyasu Award), in 2017, Achievement Award, in 2019, IEEE GRSS Education Award, in 2012, and IEEE Ulrich L. Rohde Innovative Conference Paper Awards on Antenna Measurements and Applications, in 2017. He was a member of the IEEE GRSS AdCom (2006–2014). He is a chair of IEEE Sendai section, in 2020–2021. He was an Associate Editor for the IEEE GEOSCIENCE AND REMOTE SENSING LETTERS, and a Guest Editor of the special issue of GPR2006 and GPR2010 in *Transactions on Geoscience and Remote Sensing*, and IGARSS2011, GPR2012, and GPR2014 in IEEE JOURNAL OF SELECTED TOPICS IN APPLIED EARTH OBSERVATIONS AND REMOTE SENSING. He was the chair of the IEEE GRSS Japan Chapter (2006–2007). He was the general chair of IGARSS2011 and the technical chair of GPR1996.